Delft University of Technology

Assessment of cyclic deformation behaviour of wire arc additively manufactured carbon steel

Mendez-Morales, Mariela; Branco, Ricardo; Tankova, Trayana; Rebelo, Carlos

Important note
To cite this publication, please use the final published version (if applicable).
Please check the document version above.

Assessment of cyclic deformation behaviour of wire arc additively manufactured carbon steel

Mariela Mendez-Morales [a,*], Ricardo Branco [b], Trayana Tankova [c], Carlos Rebelo [a]

[a] *University of Coimbra, ISISE, ARISE, Department of Civil Engineering, Rua Luis Reis Santos, 3030-790 Coimbra, Portugal*
[b] *University of Coimbra, CEMMPRE, ARISE, Department of Mechanical Engineering, Rua Luis Reis Santos, 3030-788 Coimbra, Portugal*
[c] *Delft University Technology, Department of Engineering Structures, Stevinweg 1, 2628 CN Delft, the Netherlands*

ABSTRACT

Wire Arc Additive Manufacturing (WAAM) has gained popularity due to its speed and cost-effectiveness. However, the current knowledge on the cyclic deformation behaviour of WAAM materials is limited. To address this issue, this study investigates the cyclic deformation behaviour of WAAM ER70S-6 carbon steel. Coupons were extracted from printed walls with horizontal and vertical orientations and from surface and interior locations. Low-cycle fatigue tests were performed under fully reversed strain-controlled conditions, spanning strain amplitudes from 0.20 % to 1.50 %. Regardless of the group, the material exhibited cyclic hardening for strain amplitudes above 0.60 % and cyclic softening for smaller strain amplitudes. Significant non-Masing hysteretic behaviour was also observed. Cyclic stress–strain curves and fatigue-life relationships written in terms of stress, strain and energy-based parameters were derived for all groups. Fatigue life was not significantly influenced by printing orientation or location across thickness. However, horizontal orientation resulted in a slightly superior fatigue response. A statistical analysis revealed no significant difference in the accuracy of fatigue-life relationships between the groups. Finally, a comparative study between WAAM materials and conventional steels showed promising results. Yet, conventional steels outperform WAAM carbon steel, at least doubling the fatigue life for the same value of the damage parameter.

1. Introduction

Additive Manufacturing (AM), often referred to as 3D printing, has evolved from its early days of rapid prototyping to a versatile technology with applications across various industries, including structural engineering [1–3]. The procedure involves adding material layer by layer to produce new features. It opens up the possibility of creating optimised designs that would be too challenging or even impossible to manufacture using conventional technologies [4–7].

Metal Additive Manufacturing, a specialised category within the broader AM domain, employs advanced techniques like Powder Bed Fusion (PBF) and Direct Energy Deposition (DED) to create intricate forms. In particular, Wire Arc Additive Manufacturing (WAAM), an important member of the DED family, has emerged as one of the leading methods for producing large steel components. Its widespread adoption can be attributed to high deposition rates, allowing for open fabrication environments, cost-effectiveness, and environmental benefits [8–11].

However, WAAM still faces obstacles in achieving high-quality final products. Many of these challenges are inherited from the rapid cooling associated with welding, which can lead to residual stresses, distorted geometry, uneven surface finish, waviness, microstructure heterogeneities and inconsistent material properties. Moreover, the mechanical properties of WAAM are also influenced by factors such as wire feed rate, arc current, interpass temperature, torch speed, among others [12–15]. Ongoing scientific efforts aim to address these challenges, involving process calibration, evaluating parameter-microstructure-property relationships, and developing data-driven models for predicting material properties [16–18].

Since WAAM components are notably susceptible to fatigue failure due to the issues previously mentioned that make them vulnerable to cyclic plastic accumulation, the potential of this technology has been hindered by limited research into its fatigue performance, especially under strain-controlled conditions. Low cycle fatigue (LCF) is generally associated with high levels of stress amplitude, resulting in large values of cyclic plastic strain that can lead to fatigue failure after a low number of loading cycles. In contrast, high cycle fatigue (HCF) is characterised

---

* Corresponding author.
  E-mail address: mendezmorales@dec.uc.pt (M. Mendez-Morales).

by low levels of stress amplitude, developing almost exclusively in the elastic regime, and allowing for potentially infinite fatigue life. Material imperfections during manufacturing can trigger LCF, leading to significant damage under normal operating conditions. Hence, understanding these features is vital for mitigating the risk of fatigue failure in critical components, ensuring the robust performance of WAAM parts, and enabling the use of this technology in structures subjected to time-varying loading, such as wind-supporting structures or offshore applications [19]. This information is also fundamental for modelling the cyclic elastic–plastic behaviour of WAAM carbon steel, allowing better fatigue lifetime prediction.

The study of fatigue behaviour on WAAM materials has advanced in recent years, with a primary focus on stainless steel [20–22] and titanium alloys [23–25], among others [26–28]. However, very little research has been conducted on low-carbon steel, namely the grade ER70S-6 according to the American Welding Society (AWS) specification [29] or G3Si1 as per the International Organization for Standardization (ISO) [30]. Moreover, when focusing on low-carbon steel, most of the existing studies were devoted to the HCF regime [31–33].

Regarding LCF of low-carbon steel, Zong et al. [34] have analysed rectangular cross-section WAAM coupons in both as-built and machined conditions. The coupons were cut in three orientations relative to the printing trajectory (0°, 45°, and 90°), but only coupons cut at 90° were analysed with a machined surface finish. The testing was performed under constant-amplitude loading, followed by the derivation of cyclic stress–strain curves and strain-life relationships. The findings indicated that the as-built coupons exhibited weakened LCF properties compared to their machined counterparts. Likewise, Wang et al. [35] have tested WAAM carbon steel rectangular coupons cut in a vertical orientation. The study utilised coupons with two nominal thicknesses and two distinct surface finishes – as-built and machined – subjecting them to ten different loading scenarios. The primary objective of this investigation was to evaluate the impact of the loading scenario on the fatigue response of the various coupon sets. The study's conclusions highlighted the exceptional ductility exhibited by the material under cyclic loading and emphasised the significant dependence of the cyclic performance on both strain amplitude and strain history. This investigation was recently expanded in the research article by Wang et al. [36] by developing a modified Chaboche model to describe the cyclic constitutive behaviour of WAAM carbon steel.

These previous studies derived strain-life relationships [34,35]. Nevertheless, stress-life and energy-life relationships are important tools in the design of critical engineering components against fatigue failure. Particularly in the case of WAAM materials, these features are directly linked to the printing strategy and degree of anisotropy, both of which affect the cyclic deformation response. Thus, this paper aims to fill such gaps by investigating the LCF behaviour of WAAM ER70S-6 carbon steel in a polished surface state, considering the effect of loading orientation and location along the thickness on cyclic stress–strain response and fatigue life. Stress-life, strain-life and energy-life relationships are also derived for the different tested groups. Complementary, a comparative analysis of the LCF behaviour between WAAM carbon steel and its conventional counterpart is provided, as well as an analysis of variance (ANOVA) to assess the influence of orientation on the fatigue life relationships obtained. Finally, the fracture surfaces are examined by scanning electron microscopy to identify the main fracture mechanisms associated with the different strain levels and orientations.

2. Experimental procedure

The section is subdivided into three parts. The first outlines the fabrication strategy of WAAM carbon steel walls and presents the coupon geometry. The second describes the LCF testing procedure and the applied loading levels. The last part focuses on post-mortem examinations of the fracture surfaces to identify the failure mechanisms.

2.1. Fabrication of material coupons

The feedstock material used in this research was low-carbon AWS A5.18 ER70S-6/ISO 14341 – A – G 42 4 M21 G 3Si1 coated copper wire of 1.0 mm diameter, hereafter referred to as ER70S-6. Table 1 summarises the nominal chemical composition as a weight percentage, while Table 2 lists its main mechanical properties according to the manufacturer [37].

The fatigue coupons were extracted from three carbon steel walls produced at the AM Construction Laboratory of the University of Coimbra, two for horizontal coupons and one for vertical coupons, see Fig. 1. This task employed an ABB IRB 4600 robot paired with a CMT Fronius TPS 400i welding machine. The fabrication parameters given in Table 3 were chosen to match those used by Tankova et al. [13] to provide continuity to the work carried out by this research group. The total printing time for the three walls (also considering the time the torch was off) was 13 h, and the calibrated layer height was 2.44 mm. Fig. 1(a) illustrates the selected deposition trajectory, highlighting the welding beads' consistent longitudinal alignment. Note that the beads were deposited in an alternating pattern per layer, in both transverse and vertical directions.

Regarding the microstructure features, as previously determined by other scholars [13,32], the microstructure of WAAM ER70S-6 exhibits polygonal ferrite and intergranular lamellar perlite, indicative of conventional non-alloyed low-carbon steels. Similarly, a recent study by our research group showed a recrystallised coarse-grained structure independent of the sample's location [13]. Fig. 2 shows the prevailing microstructure characteristics observed for the tested material in the transversal and longitudinal directions, which exhibits a recrystallised coarse-grained structure with an average grain size ranging from 9 μm to 13 μm, respectively. The enlarged grain size is typically attributed to the heat sink effect resulting from heat accumulation during fabrication. The microstructure's homogeneity is likely associated with the thermal cycle reaching a steady-state condition; these conclusions are shared with previous studies on WAAM materials [38–40].

The coupons were cut using a geometry per ASTM E 606–21 [41], as shown in Fig. 1(b); the gauge sections were polished using 320, 500, 1200 and 2400 grit sandpaper and 3.0 μm diamond paste for the final finish in order to reduce the detrimental effect of surface undulations. To examine the influence of the printing strategy on the cyclic behaviour of the WAAM carbon steel, the printing strategy was defined to ensure: (i) the fabricated walls had sufficient thickness to allow the extraction of three coupons in the *x*-direction, as shown in Fig. 1; and (ii) the extraction of coupons in two different orientations, namely horizontal (*y*-direction, parallel to the deposition trajectory, as in Fig. 1(c)) and vertical (*z*-direction, perpendicular to the deposition trajectory, as shown in Fig. 1(d)). The combination of these criteria resulted in four different groups: horizontal coupons from the surface (HS), horizontal coupons from the interior (HI), vertical coupons from the surface (VS), and vertical coupons from the interior (VI). Note that the residual stress levels were not considered in this study.

2.2. Low-cycle fatigue testing

For each orientation (horizontal and vertical), a total of 18 coupons were extracted from the printed walls. Six coupons from each orientation were machined as closely as possible to the surface, while the subsequent 12 were acquired from the internal volume of the wall. This approach enables the research to identify possible orientation-dependent or thickness-dependent effects.

Uniaxial LCF tests were conducted following the procedures of ASTM E 606–21 [41] via the single-step method, in which the strain amplitude (ε_a) is maintained constant throughout the test, considering fully-reversed conditions ($R_\varepsilon = -1$), a constant strain rate ($d\varepsilon/dt$) equal to 8×10^{-3} s^{-1}, and sinusoidal waveforms. The studied strain amplitudes ranged from 0.20 % to 1.50 %, as detailed in Table 4. Note that for

Table 1
Chemical composition of ER70S-6 feedstock wire (wt.%).

Feedstock wire	C	Mn	Cr	Ni	Mo	V	P	Fe
ER70S-6	0.05 – 0.15	1.40 – 1.85	0.15 max	0.15 max	0.15 max	0.03 max	0.025 max	Bal.

Table 2
Mechanical properties of ER70S-6 feedstock wire.

Feedstock wire	Yield stress (MPa)	Ultimate tensile strength (MPa)
ER70S-6	420	520

groups HI and VI, additional strain amplitudes were tested. The experimental setup included a 100 kN DARTEC closed-loop servo-hydraulic testing machine and a 12.5 mm-gauge mechanical extensometer (Instron 2620–601 model). Two stopping conditions were defined for the tests: i) total failure and ii) 30 % load drop. An average of 200 data points were recorded per cycle during each individual test.

In addition to the testing mentioned above, as summarised in Table 4, six coupons, three for each direction, i.e. HI and VI, were subjected to uniaxial stress-controlled conditions with stress amplitudes (σ_a) spanning from 255 MPa to 305 MPa, considering a stress ratio (R_σ) of −1, a cyclic frequency of 10 Hz, and sinusoidal waveforms. In this case, tests were stopped when the specimen reached total failure, i.e. separation of the specimen into two parts.

2.3. Fractography

Following the LCF testing, the fracture surfaces were examined to understand better the failure mechanisms associated with the various groups and the strain levels. Initially, these surfaces were observed through optical microscopy (OM) with a Carl Zeiss Axiotech 100HD microscope. Later, they were subject to analysis through conventional scanning electron microscopy (SEM) imaging using a Carl-Zeiss Gemini 500 FE machine. For SEM imaging, the gauge section of the chosen

Table 3
CMT-WAAM wall fabrication parameters.

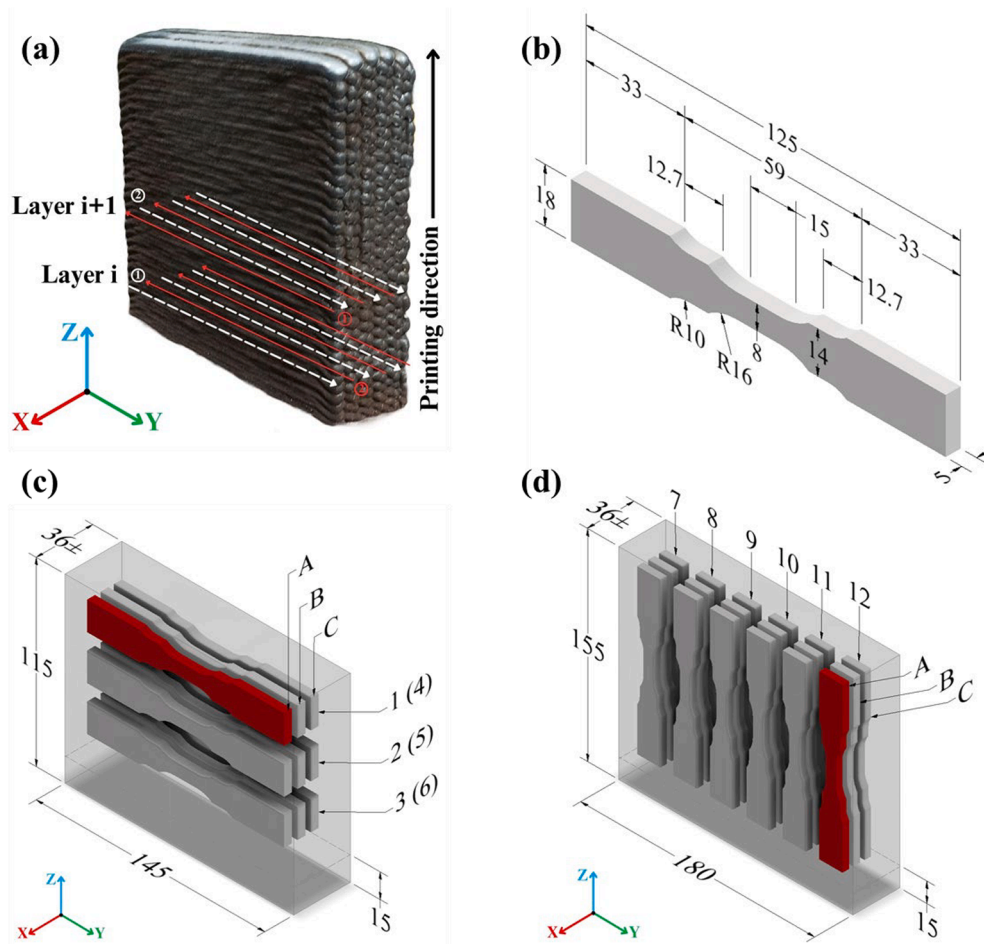| Process parameter	Detail
Current (A)	155
Voltage (V)	15.7
Wire diameter (m/min)	1.0
Wire feed (m/min)	6.0
Robot speed (mm/s)	10.0
Shielding gas	98 % Ar + 2 % CO_2 (M12)
Dwell time (s)	15
Layer height (mm)	2.44

Fig. 1. Fabrication details of the coupons (a) printing path, (b) coupon geometry, (c) walls' geometry for horizontal coupons (coupons extracted from the second wall are identified by the numbers in parentheses) and (d) wall geometry for vertical coupons (no scale, dimensions in millimetres).
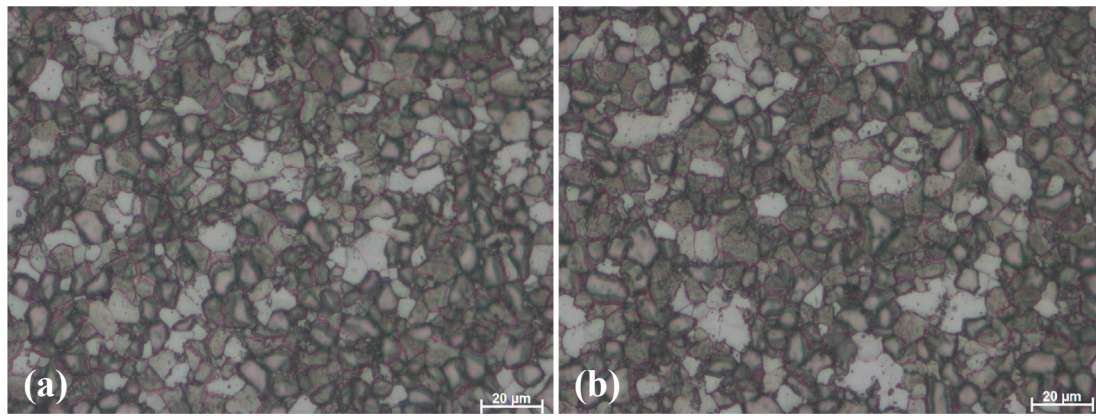
Fig. 2. Metallographic images of WAAM ER70S-6 carbon steel: (a) transversal and (b) longitudinal directions.

Table 4
Summary of low-cycle fatigue experimental campaign.

Strain-controlled tests ($R_\varepsilon = -1$)									
HS	ε_a (%)	0.20	-	0.40	-	0.60	0.80	1.00	1.25	-
HI	ε_a (%)	0.20	0.30	0.40	0.50	0.60	0.80	1.00	1.25	1.50
VS	ε_a (%)	0.20	–	0.40	–	0.60	0.80	1.00	1.25	–
VI	ε_a (%)	0.20	0.30	0.40	0.50	0.60	0.80	1.00	1.25	1.50
Stress-controlled tests ($R_\sigma = -1$)									
HI	σ_a (MPa)	295	275	255						
VI	σ_a (MPa)	305	280	255						

coupons was precision-cut using a high-speed cutting machine and thoroughly cleaned via ultrasonic treatment in a trichloroethylene solution. This analysis comprised the specimens tested at 0.20 % and 1.25 % strain amplitudes, i.e. lower and higher loading levels, across all four test groups.

3. Results and discussion

This section is subdivided into five parts. The first two parts focus on the cyclic deformation behaviour and the stable stress–strain response. After that, subsection 3.3 addresses the fatigue-life relationships for the different groups, and subsection 3.4 compares the fatigue-life relationships obtained with previous studies carried out for equivalent WAAM and conventional materials. Finally, the last subsection concludes with the analysis of failure mechanisms by OM and SEM.

3.1. Cyclic deformation behaviour

The cyclic stress–strain response for all four groups under investigation at $\varepsilon_a = 1.25$ % is illustrated in Fig. 3; results from the tensile portion of the first cycle and half-life cycle have been included to aid the analysis. The study of the complete stress–strain response shows a consistent pattern, where an increase in the maximum tensile stress evidences a strain-hardening behaviour. In addition, the overall response is relatively similar across the four cases and does not suffer significant changes during the test; the hysteresis loops have only visible differences in the plastic phase of the loading cycles.

At first glance, as shown in Fig. 3, the shape of the half-life loops collected at $\varepsilon_a = 1.25$ % seems to be similar for all groups. A more detailed analysis of these results, as exhibited in Fig. 4(a), shows a slight difference between the four cases. Withal, this difference is minimal when coupons with the same orientation are compared. Assuming the group HI as the reference case, the maximum differences between the loop's areas are lower than 2.4 %. Fig. 4(b) compares the half-life hysteresis loops for the four groups at $\varepsilon_a = 0.80$ %. Although the differences in this case are somewhat higher, there are still no relevant disparities

across the four groups. Notably, at $\varepsilon_a = 0.80$ %, the area inside the half-life loop for the group VS exceeds that of the other groups. The maximum difference between the loop's areas quantified, assuming the group HI as the reference case, was 3.4 %. In both cases, i.e. $\varepsilon_a = 1.25$ % and $\varepsilon_a = 0.80$ %, the maximum difference was attributed to group VS. This trend was also identified for other strain amplitudes.

The changes in the stress response during the tests can be better evaluated using dependent parameters. Fig. 5 exhibits the variation of stress amplitude, σ_a, with the fatigue life, N, for testing groups HI and VI as an example of the general trends. To facilitate a comparison of trends across all groups, the results for groups HS and VS are also included at a strain amplitude of 0.60 %. It can be concluded that the material displayed hardening behaviour at higher strain amplitudes, while the tendency was toward softening behaviour at lower strain amplitudes.

The cyclic stress response of the WAAM carbon steel studied in this research, see Fig. 5, encompasses the three main phases typical for most steels: an initial transient phase, a stable phase, and a final phase with sudden changes [20,26,42]. In this study, the initial response dominated approximately 10 % of the life, and the stable response persisted over the next 75 % of the life. In comparison, the final stage encompassed nearly the last 15 % of the life. Although not exactly the same, results from the WAAM carbon steel investigated relative to the cyclic stress response align with the trends found in previous research on the same material [34–36]. Fig. 5(b) shows the values obtained by Zong et al. [34] for a coupon tested at $\varepsilon_a = 1.0$ % in the machined conditions. In this case, the stress amplitude was smaller than in the current study, but both trends were similar.

To quantify the degree of cyclic hardening/softening (HS) of the different groups, the hardening ratio was determined for each cycle using the following expressions [43]:

$$HS = \frac{\sigma_{a,HL}}{\sigma_{MC}} \tag{1}$$

where $\sigma_{a,HL}$ represents the stress amplitude of the half-life cycle, and σ_{MC} denotes the stress calculated from the monotonic stress–strain curve
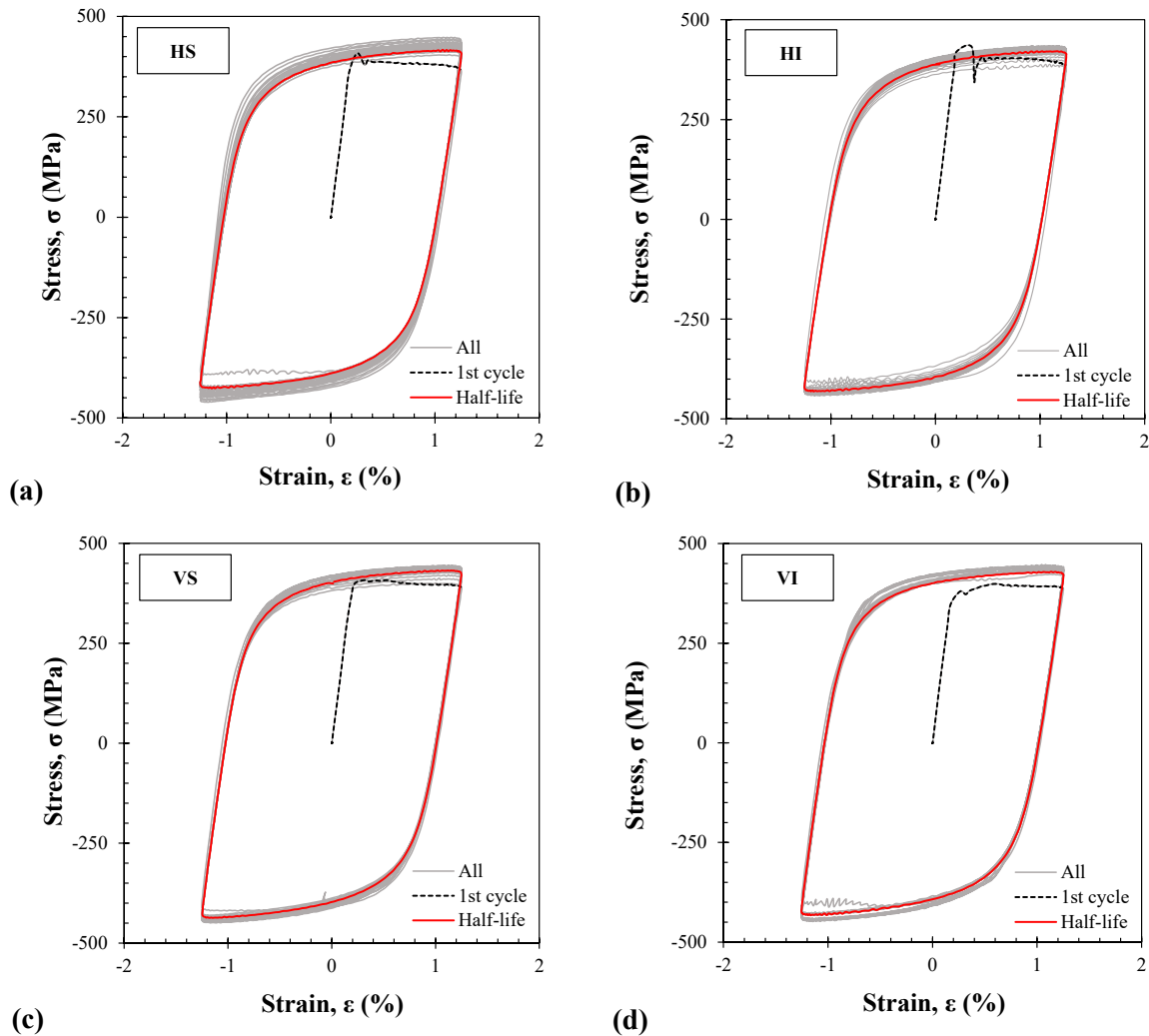
Fig. 3. Full hysteretic curves compared with the tensile portion of the first cycle and half-life cycle at $\varepsilon_a = 1.25$ % for: (a) HS, (b) HI, (c) VS, and (d) VI group.
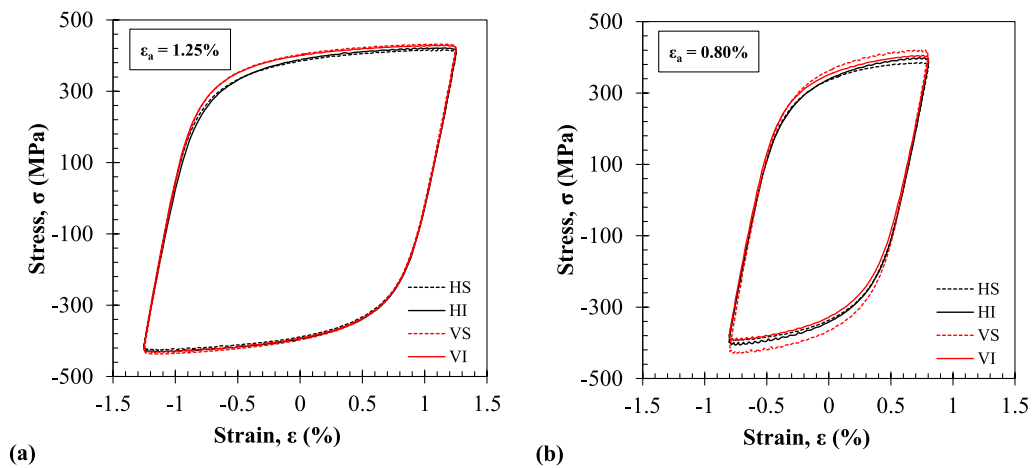

Fig. 4. General comparison of stress–strain hysteretic loops for different groups at different strain amplitudes: (a) $\varepsilon_a = 1.25$ %, and (b) $\varepsilon_a = 0.80$ %.

obtained from the loading phase of the first cycle of the LCF test at $\varepsilon_a = 1.5$ %. Based on Eq. (1), it can be concluded that $HS > 1$ for cyclic hardening behaviour and $HS < 1$ for cyclic softening behaviour. The outcomes of these calculations are presented in Fig. 6 for all groups, confirming the previously observed patterns regarding the hardening/

softening behaviour of the WAAM ER70S-6 material. This affirms that the material experiences cyclic hardening for higher strain amplitudes and cyclic softening for lower strain amplitudes. According to the fitted function for all coupons, shown in Fig. 6, the transition threshold occurs at a strain amplitude of 0.60 %. This value is nearly identical to those
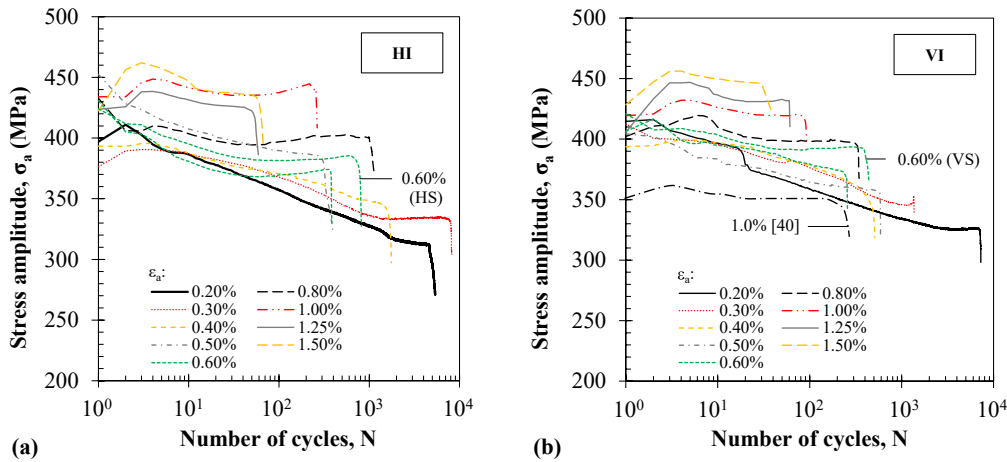
Fig. 5. Stress amplitude versus fatigue life for groups: (a) HI and (b) VI.
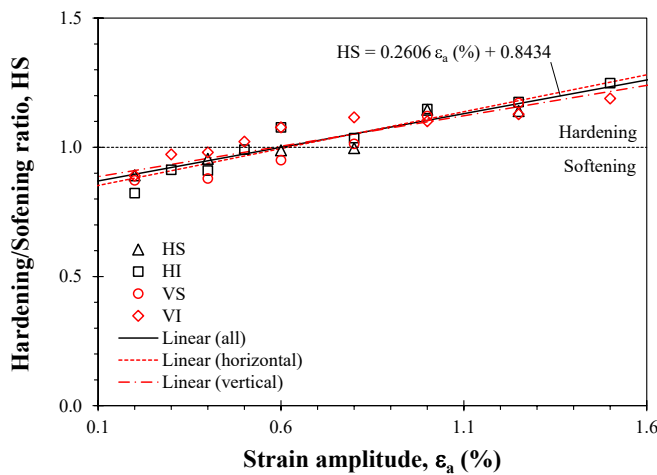

Fig. 6. Degree of cyclic hardening/softening versus strain amplitude for all groups.

obtained from the functions of the horizontal and vertical groups, which are 0.62 % and 0.58 %, respectively. This combined hardening/softening behaviour was also reported in a previous study on LCF of WAAM carbon steel by Zong et al. [34]. Hardening behaviour at higher strain amplitudes was reported by Wang et al. [36] as well. The main difference with these two prior studies lies in the defined transition threshold, previously stated at a strain amplitude of 0.50 %.

The observed hardening/softening behaviour aligns with the empirical rule proposed by Hirschberg et al. [44]. According to this model, a material's distinct responses to cyclic straining can be intuited from the ratio of ultimate stress (f_u) to yield stress (f_y) derived from monotonic tensile tests, i.e. f_u/f_y. Materials with $f_u/f_y \leq 1.2$ demonstrate softening behaviour, while those with $f_u/f_y \geq 1.4$ exhibit strain-hardening. In the intermediate range, where $1.2 < f_u/f_y < 1.4$, both hardening and softening phenomena are likely to be observed. Regarding the tested material, Tankova et al. [13] reported f_u/f_y ratios of 1.34 for horizontally machined samples and 1.33 for vertically machined samples extracted from a wall printed using the same fabrication parameters.

3.2. Cyclic stress–strain response

Based on the analyses in the previous section of this article regarding the cyclic response, it can be assumed that the material displays a stable stress–strain behaviour. Thus, as customary in many studies focused on

conventional or additively manufactured metals, the half-life cycles were used to represent the stable stress–strain response. The main variables extracted from the half-life cycles for each group are summarised in Table 5, i.e. number of reversals to failure, $2N_f$, stress amplitude, σ_a, elastic strain amplitude, $\varepsilon_{a,e}$, plastic strain amplitude, $\varepsilon_{a,p}$, total strain amplitude, ε_a, positive elastic strain energy density, ΔW_{e+}, plastic strain energy density, ΔW_p, and total strain energy density, ΔW_t. The plastic strain energy density was calculated by integrating the area of the half-life loop of each coupon. The nomenclature of the coupons is initially denoted by the group designation (HS, HI, VS, and VI), followed by the coupon number (from 1 to 12) and the specific extraction location (A, B or C) as shown in Fig. 1.

Fig. 7(a) illustrates the stabilised loops at half-life for various strain amplitudes, comparing results obtained from HS and HI groups. Analogously, Fig. 7(b) presents comparable findings for the VS and VI groups. The figures also show the respective monotonic stress–strain part obtained experimentally during the first cycle of the LCF test for ε_a = 1.5 % and the cyclic stress–strain curves represented by the full thick lines. The cyclic stress–strain curves were obtained considering all horizontal coupons (CC-H) and all vertical coupons (CC-V). Upon examination of Fig. 7, it is worth noting that the peak tensile and peak compressive points of the hysteresis loops fit the general cyclic curves well, regardless of the group. Only the case VS-8A, tested at ε_a = 1.0 %, deviates from the general trend. Thus, this test was excluded from the subsequent analyses. Furthermore, in agreement with previous findings in this work, it is visible again that WAAM coupons exhibit cyclic hardening in both horizontal and vertical orientations when subjected to strain amplitudes equal to or greater than 0.60 %. This is evidenced by the maximum tensile stress increasing with the increment in the strain amplitude and consistently outperforming the monotonic curve. Contrarily, the specimens undergo cyclic softening for strain amplitudes smaller than 0.60 %.

The cyclic stress–strain curves shown in Fig. 7 were calculated by the modified Ramberg-Osgood equation [45]:

$$\sigma_a = E\,\varepsilon_{a,e} + k'\left(\varepsilon_{a,p}\right)^{n'} \tag{2}$$

where E is the Young's modulus for each condition (201.1 GPa and 237.1 GPa for horizontal and vertical coupons, respectively), $\varepsilon_{a,e}$ is the elastic strain range, $\varepsilon_{a,p}$ is the plastic strain range, k' is the cyclic hardening coefficient, and n' is the cyclic hardening exponent. The power law proposed by Morrow [46], relating the stress amplitude and the plastic strain amplitude, was used to determine the fitting coefficients.

Table 6 presents these fitting constants alongside their respective correlation coefficients for each individual group and three additional conditions: all horizontal coupons, all vertical coupons, and the entire

Table 5
LCF results for WAAM ER70S-6 carbon steel coupons.

ID	$2N_f$ (reversals)	σ_a (MPa)	$\varepsilon_{a,e}$ (%)	$\varepsilon_{a,p}$ (%)	ε_a (%)	ΔW_{e+} (MJ/m³)	ΔW_p (MJ/m³)	ΔW_t (MJ/m³)
HS-6A	54,098	321.5	0.159	0.052	0.211	0.497	0.593	0.854
HS-5A	1854	332.4	0.164	0.241	0.405	0.417	2.367	2.698
HS-4A	1676	383.3	0.190	0.414	0.603	0.425	5.356	5.734
HS-3A	1008	389.2	0.193	0.611	0.803	0.377	7.839	8.264
HS-1A	324	404.5	0.200	0.802	1.003	0.331	11.374	11.791
HS-2A	206	421.8	0.209	1.045	1.253	0.260	15.349	15.846
HI-4C	11,246	314.2	0.155	0.055	0.211	0.525	0.536	0.795
HI-4B	16,758	334.2	0.165	0.144	0.310	0.487	1.543	1.824
HI-1C	3544	348.9	0.173	0.233	0.406	0.486	2.606	2.916
HI-3C	894	387.0	0.192	0.313	0.505	0.439	4.000	4.374
HI-2B	770	371.2	0.184	0.420	0.604	0.354	5.290	5.644
HI-2C	2478	402.3	0.199	0.605	0.804	0.374	7.991	8.430
HI-3B	540	437.4	0.216	0.786	1.003	0.310	12.078	12.564
HI-5B	130	426.3	0.211	1.042	1.253	0.281	15.485	15.972
HI-5C	140	437.2	0.216	1.286	1.502	0.260	19.583	20.108
HI-6C	156,938	295.0	0.146	0.040	0.186	0.275		0.275
HI-6B	188,540	275.0	0.136	0.022	0.158	0.217		0.217
HI-1B	2,754,770	255.0	0.126	0.011	0.138	0.175		0.175
VS-12A	8114	331.1	0.140	0.059	0.199	0.538	0.448	0.731
VS-10A	6256	355.1	0.150	0.249	0.398	0.500	2.609	2.932
VS-11A	1010	393.7	0.166	0.433	0.599	0.487	5.562	5.942
VS-7A	1776	425.4	0.179	0.619	0.798	0.471	8.513	8.970
VS-8A*	16	462.0	0.195	0.808	1.003	0.436	13.567	14.053
VS-9A	86	434.6	0.183	1.066	1.249	0.373	15.852	16.367
VI-8B	14,888	325.6	0.137	0.075	0.212	0.337	0.566	0.822
VI-7C	2738	349.1	0.147	0.162	0.309	0.306	1.430	1.736
VI-9B	1158	362.6	0.153	0.253	0.406	0.256	2.677	3.014
VI-9C	1196	360.9	0.152	0.351	0.504	0.515	3.697	4.070
VI-10B	530	376.5	0.159	0.446	0.605	0.486	4.977	5.413
VI-10C	780	399.4	0.168	0.634	0.803	0.457	7.949	8.420
VI-7B	306	419.5	0.177	0.826	1.003	0.380	11.305	11.792
VI-8C	122	431.0	0.182	1.071	1.253	0.323	15.798	16.298
VI-11C	82	446.9	0.189	1.313	1.501	0.282	20.244	20.782
VI-11B	89,108	305.0	0.129	0.052	0.1802	0.275		0.275
VI-12B	105,520	280.0	0.118	0.024	0.1419	0.197		0.197
VI-12C	593,878	255.0	0.108	0.010	0.1177	0.150		0.150

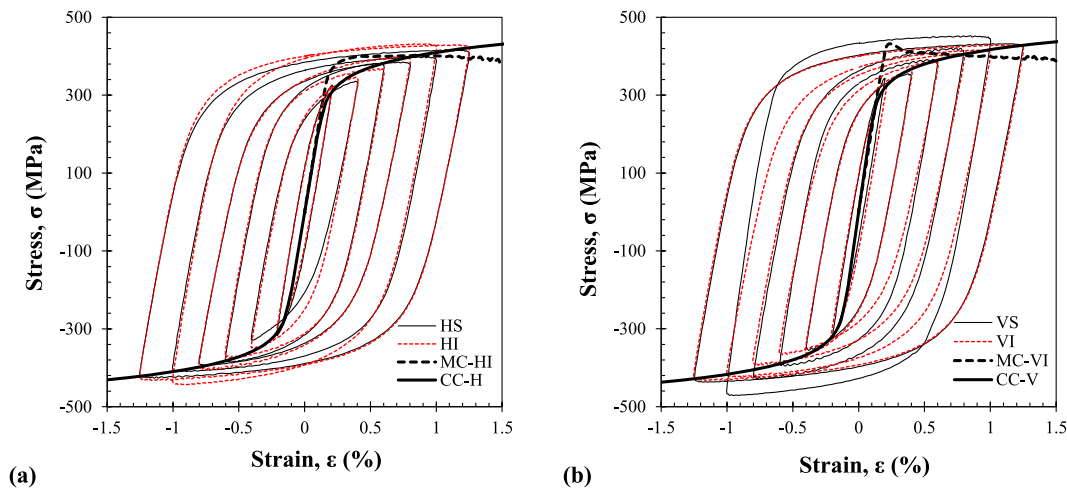*Coupon excluded from fitting curves.

Fig. 7. Stabilised hysteresis loops for (a) horizontal and (b) vertical coupons and cyclic (CC) stress–strain curves. CC-H refers to all horizontal coupons, while CC-V refers to all vertical coupons.

population of coupons, irrespective of their orientation. For all cases, the correlation coefficients were very satisfactory. It can also be concluded that the k' and n' values did not show significant variations and are relatively close for all groups, agreeing with the previous observations. The maximum absolute difference between the k' value fitted using all coupons and that fitted using horizontal or vertical coupons was lower than 0.49 %. Regarding n', the maximum absolute difference was

approximately 0.57 %.

Understanding the shape of hysteresis loops holds crucial importance in the context of energy-based approaches. Fig. 8 plots the half-life loops for the two expanded groups, i.e. all horizontal and all vertical coupons, in relative coordinates, with the lower tips connected. When the loops are joined at the lower tip, it becomes apparent that the upper branches for different strain amplitudes do not follow a single trajectory,

Table 6
Cyclic mechanical properties of WAAM ER70S-6 carbon steel.

Group	R^2	k' (MPa)	n'
HS	0.868	629.082	0.0931
HI	0.931	725.927	0.1151
VS	0.916	686.974	0.1012
VI	0.952	704.044	0.1105
Horizontal (all)	0.893	684.036	0.1060
Vertical (all)	0.920	690.214	0.1051
ALL	0.902	687.390	0.1057

deviating from the Masing curve. In a perfectly Masing material, the upper branches would replicate the path of the Masing curve [47]. The Masing curve was constructed by scaling the strains and stresses of the cyclic curve by a factor of two. Cyclic curves of Fig. 8(a) and Fig. 8(b) were calculated by means of Eq. (2) using the coefficients of Table 6 for all horizontal coupons and all vertical coupons, respectively.

The analysis of hysteresis loop shapes, as seen in Fig. 8, revealed that WAAM ER70S-6 carbon steel displayed non-Masing behaviour, especially at higher strain amplitudes, a characteristic often associated with alterations in the linear range of stable loops [48]. These alterations result from changes in microstructure induced by the applied cyclic strain, which affects the cell structure and eases the motion of dislocations [49]. It is clear that at strain amplitudes greater or equal to 0.50 %, both the microstructure and the dislocation structure are not stable. On the contrary, the material displays Masing behaviour at lower strain amplitudes. This is expected since conventional or additively manufactured ferrite-pearlite microstructures exhibit Masing behaviour at low-strain amplitudes and non-Masing behaviour at large strain amplitudes [34,50].

3.3. Fatigue-life relationships

Fatigue-life relationships describe the link between fatigue life, often represented as the number of reversals to failure and a particular variable. These relationships are crucial in engineering design to account for the effects of fatigue damage on components or structures. Here, three models to define such relations are explored in detail: the Basquin-Coffin-Manson (BCM) model, the Smith-Topper-Watson (SWT) model, and the Total Strain Energy Density (TSED) model.

3.3.1. Basquin-Coffin-Manson model

Strain-life relationships are commonly employed in the fatigue design of engineering structures subjected to time-varying loading. The BCM model is often used to represent the relationship between the total strain amplitude and the number of reversals to failure [51–53]:

$$\varepsilon_a = \varepsilon_{a,e} + \varepsilon_{a,p} = \frac{\sigma_f'}{E}(2N_f)^b + \varepsilon_f'(2N_f)^c \tag{3}$$

where σ_f' is the fatigue strength coefficient, b is the fatigue strength exponent, ε_f' is the fatigue ductility coefficient, and c is the fatigue ductility exponent. These four constants can be found through a linear regression process, plotting both plastic and elastic strain amplitudes against the number of reversals to failure on log–log scales. A summary of these constants and the correlation coefficients for all groups studied is found in Table 7.

Fig. 9 illustrates the BCM model compared to experimental data organised by group, more precisely, all horizontal coupons (Fig. 9(a)) and all vertical coupons (Fig. 9(b)). As anticipated, the fatigue life decreases with increasing strain amplitude. A satisfactory alignment between the fitted equations and the experimental results is observed and corroborated by evaluating the correlation coefficients. Regardless of orientation, it is evident that the location along the thickness is not a relevant variable since results from coupons extracted from surface and interior positions are perfectly arranged in the same range.

Transition life, $2N_T$, indicative of the shift from the LCF regime to the HCF regime, can be derived from Eq. (3), assuming that the magnitude of plastic strain amplitude is equal to the magnitude of elastic strain amplitude [54]. This value is significant for material selection and engineering design, as it can guide the design towards an elastic or plastic approach. Fig. 9 illustrates the transition life results for both horizontal and vertical groups. Notably, both groups exhibit similar transition life, with horizontal coupons prolonging the predominant plastic phase throughout a few more cycles, less than 3 %, in the fatigue life.

In the prior study by Tankova et al. [13], vertical coupons exhibited a negligible difference in yield strength compared to horizontal coupons, 375.7 MPa and 373.2 MPa, respectively. In the present study, horizontal coupons showed a slim improvement in fatigue life over vertical ones, in agreement with the observation that materials with higher yield

Table 7
Fatigue-strength and fatigue-ductility parameters of WAAM ER70S-6 carbon steel.

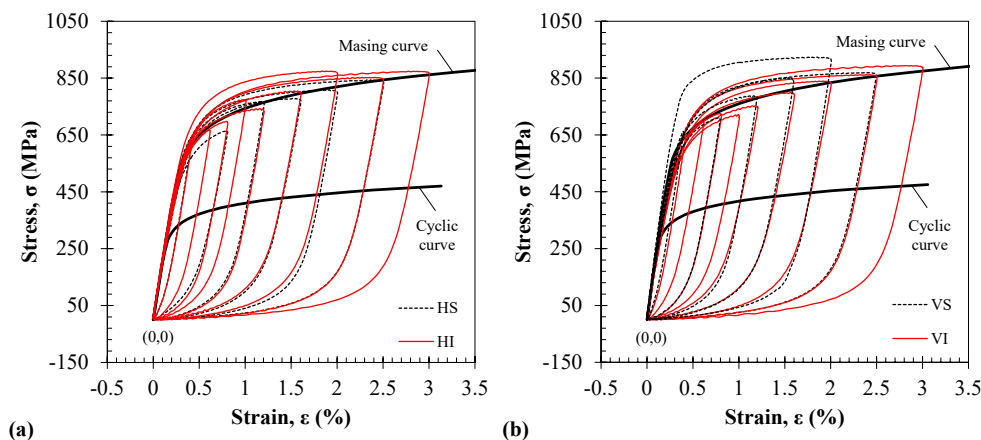| Group	R_e^2	R_p^2	σ_f' (MPa)	b	ε_f'	c
HS	0.780	0.945	575.79	−0.057	0.2002	−0.5450
HI	0.910	0.894	532.85	−0.049	0.1290	−0.4923
VS	0.682	0.824	571.18	−0.060	0.1322	−0.5022
VI	0.962	0.956	570.67	−0.053	0.1497	−0.5404
Horizontal (all)	0.888	0.905	564.40	−0.055	0.1425	−0.5022
Vertical (all)	0.897	0.901	579.83	−0.060	0.1550	−0.5390
ALL	0.891	0.885	570.50	−0.057	0.1435	−0.5154

Fig. 8. Half-life loops at different strain amplitudes with lower tips tied together and superimposed with their respective Masing and cyclic curves for groups (a) Horizontal (all) and (b) Vertical (all).
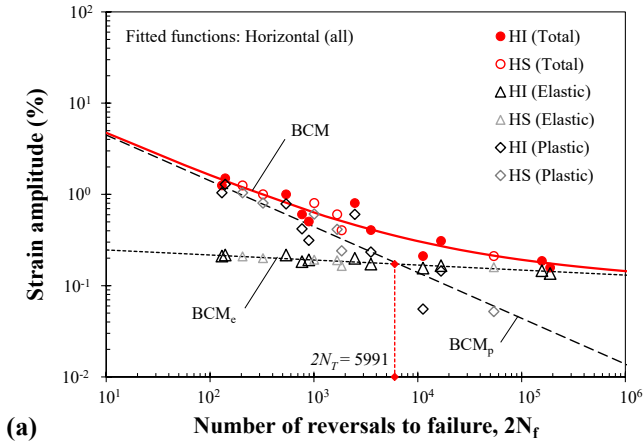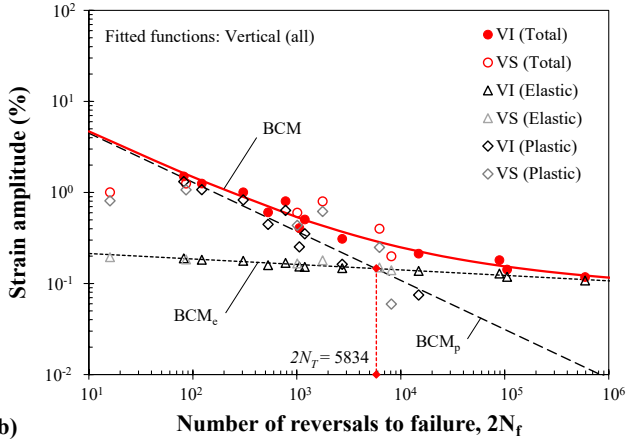
Fig. 9. Strain-life relations versus experimental data grouped by orientation for (a) horizontal and (b) vertical groups. BCM$_e$ represents the elastic component, and BCM$_p$ represents the plastic components of the BCM model.

Fig. 10. SWT-life relations versus experimental data grouped by orientation for (a) horizontal and (b) vertical groups. SWT$_e$ represents the elastic component, and SWT$_p$ represents the plastic component of the SWT model.

strength often display reduced fatigue life. Zong et al. [34] reported a similar trend for horizontal and vertical coupons made of WAAM ER70S-6 carbon steel and tested in the as-built condition. Similarly, the former led to higher fatigue life than the latter, regardless of the strain amplitude, mainly attributed to the undulating effect associated with the surface condition.
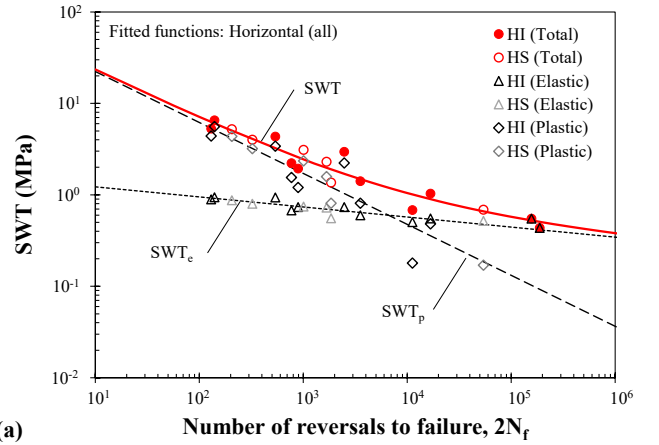
3.3.2. Smith-Watson-Topper model

The SWT is one of the most widely used models in fatigue design problems [55]. It relates the product of the maximum tensile stress, σ_{max}, and the strain amplitude, ε_a, with the number of reversals to failure, as shown in Eq. (4):
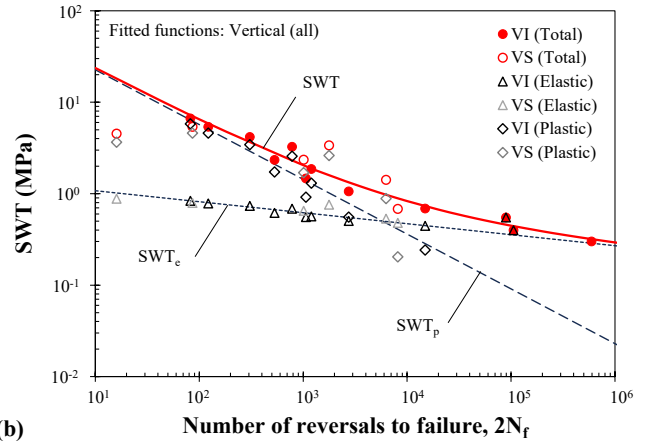
$$\sigma_{max}\,\varepsilon_a = \sigma_{max}\,\varepsilon_{a,e} + \sigma_{max}\,\varepsilon_{a,p} = \frac{\sigma_f'^{\,2}}{E}(2N_f)^{2b} + \sigma_f'\varepsilon_f'(2N_f)^{b+c} \quad (4)$$

where σ_{max} represents the maximum stress of the loading cycle. The rest of the constants are the same fatigue-strength and fatigue-ductility coefficients previously defined and summarised in Table 7. The SWT model assumes that the product $\sigma_{max}\,\varepsilon_a$ remains constant at a given life and uses this parameter as a damage indicator. Its final form is generally defined either as a stress or energy quantity [56].

The results of the SWT models for horizontal and vertical coupons are compared with the respective data points in Fig. 10. As can be seen, the functions derived from all horizontal coupons (Fig. 10(a)) and the functions derived from all vertical coupons are in good agreement with the experimental results. Moreover, it is also evident that the results of both interior and surface coupons are not affected by the location along the thickness, regardless of the strain amplitude.

3.3.3. Total strain energy density model

Energy-based models, where the dissipated strain energy density per cycle is considered the primary contributor to fatigue damage, are efficient approaches to estimating fatigue life. The TSED is one of the most popular because, in general, it provides satisfying estimations in both the LCF and HCF regimes and is sensitive to mean stress effects [57,58]. Recently, Liao et al. [59] introduced an interesting approach based on a double power function, similar to Eq. (3) and Eq. (4), that addresses the positive elastic and the plastic components separately. This model can be mathematically expressed as follows:

$$\Delta W_t = \Delta W_{e+} + \Delta W_p = E_{e+}(2N_f)^{b_{e+}} + E_p(2N_f)^{c_p} \quad (5)$$

where E_{e+} and b_{e+} are the energy-based fatigue strength coefficient and exponent, and E_p and c_p are the energy-based fatigue ductility coefficient and exponent, respectively [60]. These two pairs of constants can also be fitted independently through linear regression by plotting the positive elastic component against the number of reversals to failure and the plastic component against the number of reversals to failure on log–log scales. The constants for each energy component are listed in Table 8, alongside the correlation coefficients.

Fig. 11 shows the fitted functions for all horizontal (Fig. 11(a)) and all vertical (Fig. 11(b)) coupons, as well as the experimental results. Overall, this model demonstrates good agreement with the data points, regardless of the location of the coupons along the thickness. The resulting fitting curves agree well with the experimental results, particularly near the upper and lower limits of the tested values of the total strain energy density, i.e. when the TSED is higher or lower. At intermediate energy levels, the degree of scatter slightly increased. This

Table 8
Energy-based fatigue parameters of WAAM ER70S-6 carbon steel.

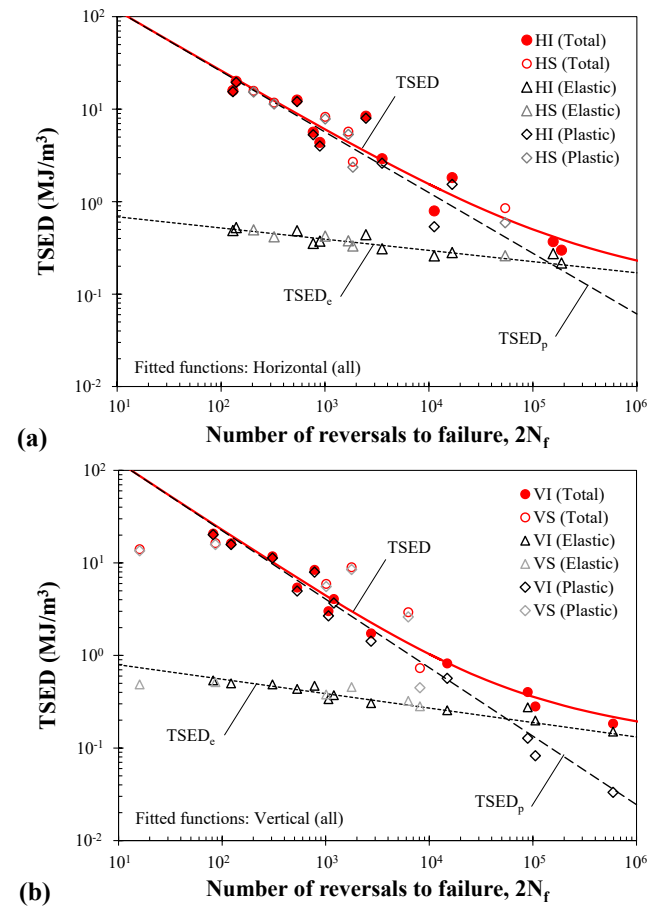| Group	R_e^2	R_p^2	E_{e+} (MJ/m³)	b_{e+}	E_p (MJ/m³)	c_p
HS	0.8798	0.951	0.8343	−0.1087	353.47	−0.5919
HI	0.903	0.875	1.0406	−0.1421	522.28	−0.6580
VS	0.768	0.949	0.9113	−0.1188	665.92	−0.7526
VI	0.921	0.886	0.9836	−0.1342	693.59	−0.7441
Horizontal (all)	0.901	0.899	1.0148	−0.1381	512.83	−0.6520
Vertical (all)	0.890	0.885	0.9854	−0.1330	533.30	−0.7029
ALL	0.886	0.850	0.9869	−0.1336	540.69	−0.6829

Fig. 11. TSED-life relations versus experimental data grouped by orientation for (a) horizontal and (b) vertical groups. TSED$_e$ represents the positive elastic component, and TSED$_p$ represents the plastic component of the TSED model.

effect is more pronounced for the coupons extracted from interior locations in the horizontal group and for the coupons extracted from the surface in the vertical group. It is also worth noting that the fitted constants, as shown in Table 7, do not exhibit significant differences among the cases associated with horizontal group, vertical group, or all tested coupons.

3.4. Assessment of fatigue-life prediction models

Two approaches are used to assess the fit of the life-prediction models developed (BCM, SWT, and TSED). The first approach compares the fatigue performance of WAAM carbon steel with other additively manufactured and conventional steels. The second approach uses statistical tools, i.e. a one-way ANOVA, to determine if the difference in the fitting constants obtained for each group, separated by orientation,

holds significance in the life prediction.

3.4.1. Comparison with previous studies

This section compares the results from the present study with other studies carried out using either additively manufactured or conventional steel materials. Previous studies reported that WAAM ER70S-6 carbon steel meets the minimum requirements of conventional S355 structural steel [13]. Hence, the LCF performance of WAAM ER70S-6 carbon steel is compared with two sets of experimental results available in the literature: WAAM machined coupons made of ER70S-6 steel extracted in the vertical direction [34] and both S355 and S690 structural steel plates produced by conventional processes [61].

Fig. 12 compares the fatigue performance of the WAAM ER70S-6 carbon steel studied in this research with the other steels reported above [34,61]. This comparative analysis is conducted through the three fatigue damage models addressed in the previous section, i.e. BCM (Fig. 12(a)), SWT (Fig. 12(b)) and TSED (Fig. 12(c)) models. In order to facilitate a more comprehensive comparison of the fatigue performance based on the coupon's orientation of the tested WAAM carbon steel, fitted functions for all specimens, as well as separate functions for all horizontal and all vertical coupons, are presented.

Regarding the strain-life data, as shown in Fig. 12(a), it can be observed that the studied material displays inferior LCF behaviour compared to conventional structural steels. In the range of 10^1 to 10^6 of $2N_f$, conventional S355 steel displays an average increase in fatigue life of 2.46 times, compared to the WAAM carbon steel of this study when subjected to the same strain amplitude. However, this lower performance tends to be mitigated as the strain amplitude decreases. For fatigue lives greater than approximately 10^5 reversals, a noteworthy similarity is displayed between the curves derived from this study and those proposed by de Jesus et al. [61] for S355 structural steel. Nevertheless, the fatigue scatter of the latter steel is slightly lower, which can be explained by the manufacturing process.

Concerning the results of the WAAM ER70S-6 carbon steel provided by Zong et al. [34], two different trends can be identified. At higher levels of plastic strain, $2N_f < 10^3$ reversals, the material used by Zong et al. [34] presents a better fatigue performance. However, after this point, the additively manufactured steel considered in this research presents better fatigue resistance. The surface condition, polished instead of machined, can help explain this phenomenon, as the HCF regime is more sensitive to surface finishing than the LCF regime. In addition, it is interesting to note that the three functions derived for the BCM model (full black and dashed red lines) are almost identical, as already anticipated. Nevertheless, it is clear that the coupons extracted horizontally lead to slightly higher fatigue lives.

Fig. 12(b) shows the data relative to the SWT model, and the overall comparison yields analogous conclusions to those obtained from the strain-life results. However, a more pronounced deviation becomes clear concerning the S690 steel relative to the additively manufactured materials, particularly at a higher number of reversals to failure. This behaviour can be explained by the different failure mechanisms occurring in the elastic-dominated and plastic-dominated regimes. Fatigue crack nucleation is associated with the formation of dislocation cells inside the plastic zone. In the elastic-dominated regime, with stress amplitude below the yield point, plastic deformation is limited to a small number of grains. The stress amplitude must reach a threshold value above which the plastic zone is created, leading to the initiation of microscopic cracks, while the material remains globally in the elastic state. In the plastic-dominated regime, generalised cyclic plasticity is likely to occur, particularly near internal defects, whose shape, size, location, and number can vary, causing some scatter in the fatigue performance.

Furthermore, similar to the preceding analysis based on the strain amplitude, the SWT data points of this work closely mirror those found by de Jesus et al. [61] for S355 steel, with S355 steel increasing the fatigue life by a factor of 3.41 on average for the same SWT damage
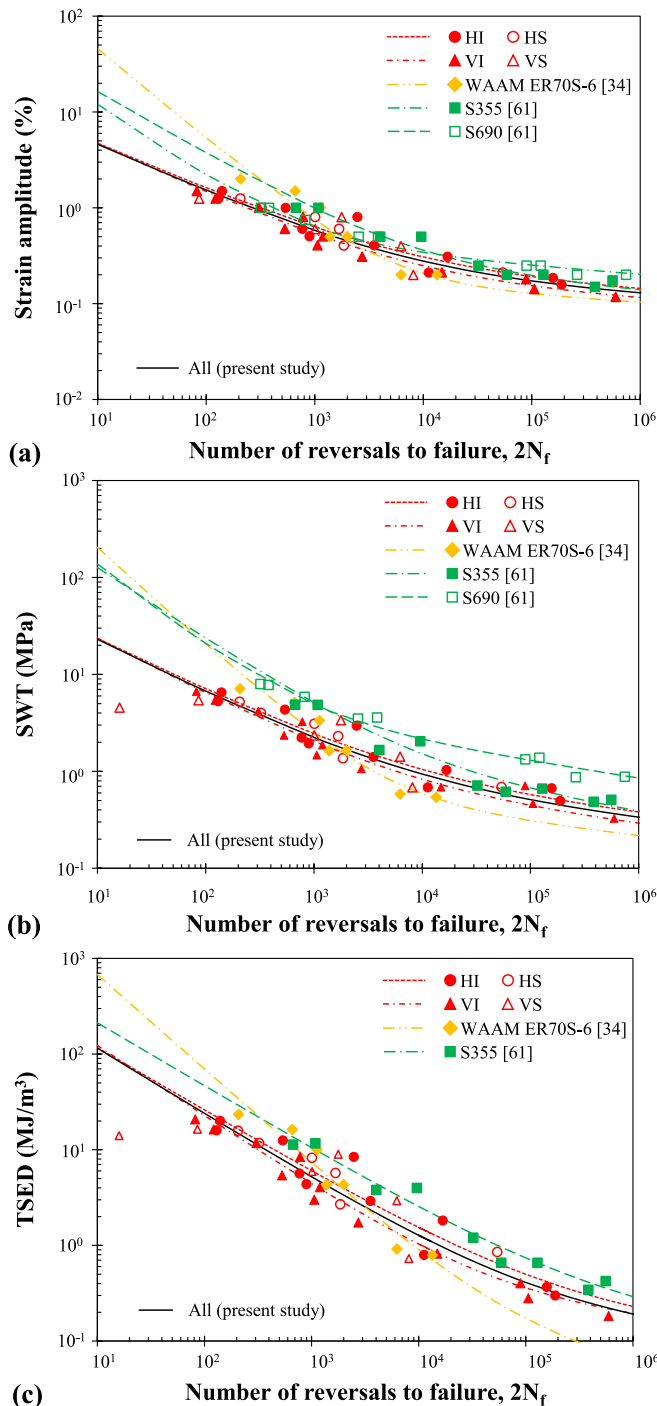
(a)

(b)

(c)

Fig. 12. Comparison of fatigue performance between the tested WAAM ER70S-6 carbon steel and other conventional and additively manufactured steels: (a) strain-life relations, (b) SWT-life relations, and (c) energy-life density relations.

parameter in the range of 10^1 to 10^6 of $2N_f$; moreover, the fatigue scatter is more significant for the WAAM carbon steel. Once again, when comparing both additively manufactured ER70S-6 carbon steels, a turning point is identified at 10^3 cycles to failure. Beyond this threshold, the material tested in this study shows superior fatigue performance, while the opposite scenario is observed for lower lives. Although the horizontal coupons again show a slightly higher fatigue resistance, the differences relative to the vertical coupons or all coupons are not significant.

Fig. 12(c) compares the TSED-life data obtained in this study with

those collected from the literature. A more significant scatter is observed in the results than in the analysis performed through the previous two fatigue damage parameters analysed. Nevertheless, the main conclusions prevail: no relevant differences were observed in the fitted curves for the three conditions defined in this study (horizontal, vertical, and all coupons); the horizontal group led to a slightly better fatigue performance; at a fatigue life higher than 10^3 cycles, the additively manufactured carbon steel studied surpassed the fatigue behaviour of WAAM ER70S-6 steel reported in the literature, and vice-versa. The curve fitted for S355 steel exhibits a similar shape to those derived for the additively manufactured carbon steel but is shifted upward. Likewise, conventional S355 steel extended the fatigue life an average of 2.74 times in the $2N_f$ range from 10^1 to 10^6 when subjected to the same value of TSED.

In summary, the three models provided good predictions of the LCF life for the studied WAAM material. Furthermore, there is a good agreement between the current experimental results and those found in the literature for the same material. Although conventional steels (S355 and S690) outperformed the fatigue results of the additively manufactured material examined in this study, the differences tend to be mitigated in the elastic-dominated region, making the WAAM ER70S-6 carbon steel a promising option for structural components subjected to fatigue loading. Despite the horizontal orientation resulting in slightly superior LCF behaviour, agreeing with the literature, the coupon orientation seems to have no significant effect on the results.

3.4.2. Statistical assessment

A statistical study based on a one-way ANOVA was performed to better analyse the effect of coupon orientation on fatigue-life predictions. Other scholars have utilised this method to assess the influence of different independent variables, such as post-processing treatments or printing orientation, on the fatigue behaviour of conventional [62] and additively manufactured materials in both LCF and HCF regimes [63–66].

The ANOVA test is widely used to determine whether the means of independent groups are statistically equal or not. In this test, the significance level, denoted as α, represents the probability of concluding that there is a significant difference when actually none exists. The *F-statistic* indicates the ratio of mean variation between groups to mean variation within groups, and *F-Fisher* denotes the variance ratio at the significance level α. Hence, an *F-statistic* smaller than *F-Fisher* suggests no statistically significant difference between the groups' means. Similarly, if the *p-value* exceeds the commonly accepted limit of $\alpha = 0.05$, the difference in means between groups lacks statistical significance [67]. It is essential to disclose that the data of this research does not follow a normal distribution. However, previous studies have demonstrated that the ANOVA is a robust statistical tool, even when normality requirements are not met [68].

Since for each model (BCM, SWT and TSED), several fitting equations were developed by grouping the experimental data under different criteria (see Table 7 and Table 8), this analysis pretends to compare such equations and define if orientation significantly affects the models. For each predictive model, three equations are compared: the equation obtained considering only horizontal coupons (H), the equation that resulted from only vertical coupons' data (V) and a final equation that accounted for all the coupons (A). For this ANOVA test, the relative error between the entire pool of experimental values, regardless of orientation, and the predicted values, using the abovementioned equations, was utilised as the source of variation.

Taking the BCM model as an example, the influence of orientation over the model was assessed by calculating the total strain amplitude using Eq. (3) with the constants from Table 7 for the H, V and A groups. This calculation was done for each coupon's number of reversals to failure ($2N_f$ in Table 5), regardless of whether they corresponded to the same group as the equation under scrutiny; this method allowed for a cross-revision of the equations, i.e. predicting the strain amplitude of vertical coupons using an equation that was calibrated using solely

horizontal coupons, and analogously for the other combinations.

Later, the relative error was computed, considering the experimental measurements of strain amplitude as true values. With the relative errors of each group for the BCM model, a one-way ANOVA was performed, obtaining ($F(2, 102) = [1.468]$, $p = 0.235$). Since the *F-statistic* (1.468) is smaller than the critical *F-Fisher* (*F-Fisher* = 3.085) and the *p-value* (0.235) exceeds the significance level ($\alpha = 0.05$), the difference between the groups is not statistically significant when estimating the fitting constants for the BCM model and defining a particular equation. In other words, regardless of the group used to obtain the fitting constants, the error in predicting the total strains is not statistically different from one group to the other. Summarised results are provided in Table 9 for the three fitted equations studied.

Analogous procedures were performed for SWT and TSED models. In the first case, i.e. the SWT model, fatigue-life predictions were obtained using Eq. (4) and the constants from Table 7. The one-way ANOVA resulted in ($F(2, 102) = [1.646]$, $p = 0.198$). In the second case, i.e. the TSED model, Eq. (5) was used alongside the constants from Table 8. The one-way ANOVA for this case was ($F(2, 102) = [0.535]$, $p = 0.587$). Thus, as in the BCM model, *F-statistic < F-Fisher* and *p-value > α*. Therefore, the *F-statistic* and *p-value* show no statistically significant difference between the relative errors of any of the groups.

This analysis reaffirms the previous observations that the orientation-dependent properties of the material have little influence on the fatigue behaviour of the studied population. Nevertheless, it is paramount to emphasise that this procedure does not identify the best-fitting equation; it merely demonstrates the absence of statistically significant differences between predictions based on group classification. The selection of the appropriate equation depends on the specific application and the critical reasoning of the researcher.

3.5. Fracture surfaces

Fracture surfaces were examined by OM and SEM to identify the main failure mechanisms associated with the different strain levels. The SEM analysis was performed at both low-strain ($\varepsilon_a = 0.20$ %) and high-strain ($\varepsilon_a = 1.25$ %) strain amplitudes. Fig. 13 and Fig. 14 present typical OM and SEM images for representative coupons subjected to low and high-strain levels, respectively. Overall, the fracture surfaces of the tested WAAM carbon steel encompass three main zones: fatigue crack initiation, fatigue crack propagation and fracture zone, which are well identified in Fig. 13(a) and Fig. 14(a).

Regarding the fatigue crack initiation process, cracks nucleated either from the surface or from internal defects. From the 36 studied samples, only seven did not exhibit any noticeable internal defects. Fig. 13 shows an example in which the crack initiated from its corner, as denoted by the radial lines converging to the edge indicative of local irreversible plastic deformation, and then propagated inwards, resulting in a characteristic fatigue fracture.

The remaining 25 coupons exhibited at least one internal defect identified as the primary origin of crack nucleation. In isolated cases, as evidenced by Fig. 14, the failure was initiated from two separate defects and propagated until they joined, forming a distinct fatigue step. Zong et al. [34] also reported single and multi-crack initiation phenomena from the surface; however, failure caused by internal defects has not been observed. As considered in that study, the undulating geometry

associated with the as-built condition induced local stress concentrations, which may have facilitated the crack initiation from the surface.

The crack propagation region occupies most of the cross-section and is well-demarcated from the fracture zone. In contrast, the boundary between the crack initiation region and the crack propagation region was not clearly perceptible. Moreover, as expected, roughness steadily increases from the fatigue crack initiation region to the fracture zone. The oval shape of the internal defects, see Fig. 14(b), is likely to be linked to gas bubbles trapped during the fabrication of the WAAM walls [69]. These geometric irregularities, along with the presence of inclusions dispersed throughout the material (see Fig. 13(c) and Fig. 14 (c)), acted as stress concentrators, adversely affecting both the crack initiation and the crack propagation stages and, ultimately, the LCF performance of the tested material.

The surface morphology in the crack propagation region was characterised by traces of plastic deformation, ductile dimples, beachmarks, fatigue striations, and secondary cracks, as shown in Fig. 13(c). Generally, secondary cracks advance perpendicular to the main crack direction, altering the load distribution and reducing the main crack propagation rate. The fatigue striations are associated with the microscopic crack growth and can be interpreted as the distance the crack extends per cycle. The beachmarks, on the other hand, also referred to as macroscopic fatigue striations, indicate the overall progression of the crack.

Concerning fracture mechanisms, low-strain amplitudes revealed a mixed ductile–brittle failure mode, while high-strain amplitudes were predominantly governed by typical ductile features, reflected by the presence of fibrous regions, see Fig. 14(c), composed of elongated dimples with elliptical shapes characterised by varying depth, size, and orientation. These fracture mechanisms agree with the failure characteristics reported in the literature for WAAM ER70S-6 carbon steel subjected to fatigue loading [34,70].

4. Conclusions

This work investigated the cyclic deformation behaviour of WAAM ER70S-6 carbon steel. Low-cycle fatigue tests were performed under fully-reversed strain-controlled conditions, covering strain amplitudes ranging from 0.20 % to 1.50 %. Furthermore, fully-reversed stress-controlled conditions were also conducted, varying from 255 MPa to 305 MPa. Coupons were extracted from the printed wall with two orientations (horizontal and vertical) and from two locations along the thickness (surface and interior). Fatigue-life relationships and cyclic stress–strain curves were derived for all groups. ANOVA tools were used to compare the fatigue-life relationships obtained for each group. Additionally, the fracture surfaces were analysed by OM and SEM to identify the main failure mechanisms. The findings of this investigation led to the following conclusions:

- The material exhibited a mixed softening-hardening behaviour. Cyclic hardening occurred at higher strain amplitudes, greater than 0.60 %, whereas cyclic softening prevailed for strain amplitudes less than 0.60 %;
- The material displayed a non-Masing behaviour, especially at higher strain amplitudes, a characteristic often associated with alterations

Table 9
Summary of ANOVA statistical results.

$\alpha = 0.05$; *F-Fisher* = 3.085								
Life prediction model	Source	DOF	dof	SS	MS	F-statistic	p-value
BCM	Experimental error between H, V and A	2	102	0.063	0.031	1.468	0.235
SWT	Experimental error between H, V and A	2	102	0.084	0.042	1.646	0.198
TSED	Experimental error between H, V and A	2	102	0.117	0.059	0.535	0.587

DOF = degrees of freedom between groups; dof = degrees of freedom within groups; SS = sum of square; MS = mean sum of square.
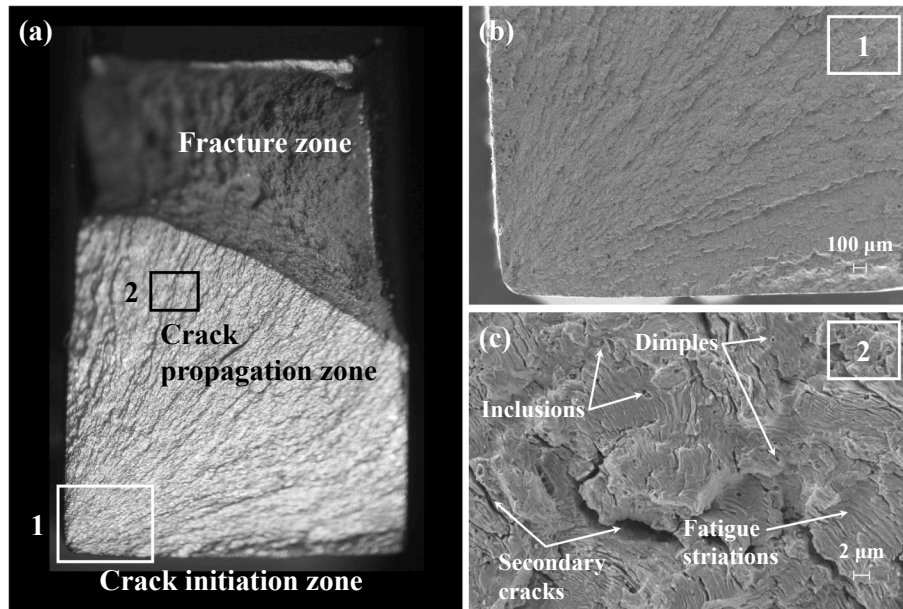
Fig. 13. Fractography of coupon HS-6A ($\varepsilon_a = 0.20$ %).
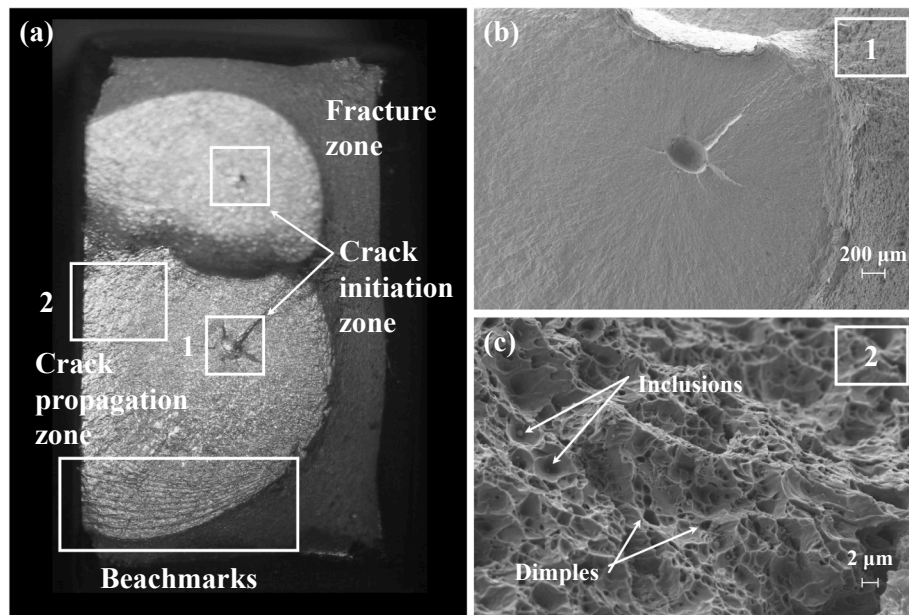

Fig. 14. Fractography of coupon HI-5B ($\varepsilon_a = 1.25$ %).

in the linear range of the stable loops, generally attributed to changes in cell structure and dislocation arrangement;

• LCF behaviour was not significantly affected by the orientation relative to the printing direction nor by location along the thickness. However, slightly better results were obtained from horizontally oriented coupons;

• The three fatigue-life prediction models (BCM, SWT and TSED) considered in this research adjusted well to the experimental observations for all groups. The ANOVA study revealed no statistically significant difference between groups relative to the fatigue-life prediction models;

• WAAM ER70S-6 carbon steel showed inferior LCF performance compared to its conventional steel counterparts. However, it aligned

with the LCF performance of WAAM carbon steel, even surpassing the literature results in the elastic-dominated regime;

• Crack initiation occurred from both the surface and internal defects caused by trapped gas bubbles during fabrication. Failure mechanisms were governed by ductile fracture at high-strain amplitudes and exhibited mixed brittle-ductile features at lower-strain amplitudes.

CRediT authorship contribution statement

Mariela Mendez-Morales: Writing – original draft, Visualization, Validation, Methodology, Investigation, Formal analysis, Writing – review & editing. **Ricardo Branco:** Conceptualization, Investigation, Methodology, Supervision, Validation, Writing – original draft, Writing

– review & editing. **Trayana Tankova:** Conceptualization, Formal analysis, Methodology, Supervision, Validation, Writing – review & editing. **Carlos Rebelo:** Writing – review & editing, Conceptualization, Formal analysis, Funding acquisition, Methodology, Supervision, Validation.

Declaration of competing interest

The authors declare that they have no known competing financial interests or personal relationships that could have appeared to influence the work reported in this paper.

Data availability

Data will be made available on request.

Acknowledgements

References

[1] Buchanan C, Gardner L. Metal 3D printing in construction: A review of methods, research, applications, opportunities and challenges. Eng Struct 2019;180:332–48. https://doi.org/10.1016/j.engstruct.2018.11.045.

[2] Galjaard S, Hofman S, Ren S. New opportunities to optimize structural designs in metal by using additive manufacturing. In: Advances in architectural geometry 2014. Springer International Publishing; 2015. p. 79–93. 10.1007/978-3-319-11418-7_6.

[3] Lange J, Feucht T, Erven M. 3D-Printing with steel-additive manufacturing connections and structures. Ce/Papers 2021;4:2–7. https://doi.org/10.1002/cepa.1258.

[4] Kanyilmaz A, Berto F, Paoletti I, Caringal RJ, Mora S. Nature-inspired optimization of tubular joints for metal 3D printing. Struct Multidiscip Optim 2021;63:767–87. https://doi.org/10.1007/s00158-020-02729-7.

[5] Mendez-Morales M, Tankova T, Branco R, Rebelo C. Additive manufacturing of a steel splice joint for tubular elements in a modular wind tower. Ce/Papers 2023;6:763–8. https://doi.org/10.1002/cepa.2729.

[6] Monteiro K, Zhu C, Tankova T, Santos AF, da Silva LS. Experimental and numerical assessment of the topological optimisation of additively manufactured T-joints. Ce/Papers 2023;6:769–74. https://doi.org/10.1002/cepa.2737.

[7] Kyvelou P, Spinasa A, Gardner L. Testing and analysis of optimized wire arc additively manufactured steel trusses. J Struct Eng 2024;150:04024008. https://doi.org/10.1061/JSENDH.STENG-12832.

[8] Dias M, Pragana JPM, Ferreira B, Ribeiro I, Silva CMA. Economic and environmental potential of wire-arc additive manufacturing. Sustainability 2022;14:5197. https://doi.org/10.3390/su14095197.

[9] Buchanan C, Matilainen V-P, Salminen A, Gardner L. Structural performance of additive manufactured metallic material and cross-sections. J Constr Steel Res 2017;136:35–48. https://doi.org/10.1016/j.jcsr.2017.05.002.

[10] Williams SW, Martina F, Addison AC, Ding J, Pardal G, Colegrove P. Wire + arc additive manufacturing. Mater Sci Technol 2016;32:641–7. https://doi.org/10.1179/1743284715Y.0000000073.

[11] Meng X, Weber B, Nitawaki M, Gardner L. Optimisation and testing of wire arc additively manufactured steel stub columns. Thin-Walled Struct 2023;189:110857. https://doi.org/10.1016/j.tws.2023.110857.

[12] Gardner L. Metal additive manufacturing in structural engineering – review, advances, opportunities and outlook. Structures 2023;47:2178–93. https://doi.org/10.1016/j.istruc.2022.12.039.

[13] Tankova T, Andrade D, Branco R, Zhu C, Rodrigues D, Simões da Silva L. Characterization of robotized CMT-WAAM carbon steel. J Constr Steel Res 2022;199. https://doi.org/10.1016/J.JCSR.2022.107624. 107624.

[14] Huang C, Kyvelou P, Gardner L. Stress-strain curves for wire arc additively manufactured steels. Eng Struct 2023;279:115628. https://doi.org/10.1016/j.engstruct.2023.115628.

[15] Mishra V, Babu A, Schreurs R, Wu K, Hermans MJM, Ayas C. Microstructure estimation and validation of ER110S-G steel structures produced by wire and arc additive manufacturing. J Mater Res Technol 2023;23:3579–601. https://doi.org/10.1016/j.jmrt.2023.01.214.

[16] Dodwell TJ, Fleming LR, Buchanan C, Kyvelou P, Detommaso G, Gosling PD, et al. A data-centric approach to generative modelling for 3D-printed steel. Proc Royal Soc A: Math Phys Eng Sci 2021;477:20210444. https://doi.org/10.1098/rspa.2021.0444.

[17] Evans S, Hadjipantelis N, Wang J. Effects of deposition rate on local stability of wire arc additively manufactured outstand elements. Ce/Papers 2023;6:678–83. https://doi.org/10.1002/cepa.2354.

[18] Hadjipantelis N, Weber B, Buchanan C, Gardner L. Description of anisotropic material response of wire and arc additively manufactured thin-walled stainless steel elements. Thin-Walled Struct 2022;171:108634. https://doi.org/10.1016/j.tws.2021.108634.

[19] Ermakova A, Mehmanparast A, Ganguly S. A review of present status and challenges of using additive manufacturing technology for offshore wind applications. Proc Struct Integrity 2019;17:29–36. https://doi.org/10.1016/j.prostr.2019.08.005.

[20] Li Y, Yuan Y, Wang D, Fu S, Song D, Vedani M, et al. Low cycle fatigue behavior of wire arc additive manufactured and solution annealed 308 L stainless steel. Addit Manuf 2022;52:102688. https://doi.org/10.1016/j.addma.2022.102688.

[21] Gordon J, Hochhalter J, Haden C, Harlow DG. Enhancement in fatigue performance of metastable austenitic stainless steel through directed energy deposition additive manufacturing. Mater Des 2019;168:107630. https://doi.org/10.1016/j.matdes.2019.107630.

[22] Xin H, Correia JAFO, Veljkovic M, Zhang Y, Berto F, de Jesus AMP. Probabilistic strain-fatigue life performance based on stochastic analysis of structural and WAAM-stainless steels. Eng Fail Anal 2021;127. https://doi.org/10.1016/j.engfailanal.2021.105495.

[23] Syed AK, Plaskitt R, Hill M, Pinter Z, Ding J, Zboray R, et al. Strain controlled fatigue behaviour of a wire + arc additive manufactured Ti-6Al-4V. Int J Fatigue 2023;171:107579. https://doi.org/10.1016/j.ijfatigue.2023.107579.

[24] Shamir M, Zhang X, Syed AK, Sadler W. Predicting the effect of surface waviness on fatigue life of a wire + arc additive manufactured Ti-6Al-4V alloy. Materials 2023;16:5355. https://doi.org/10.3390/ma16155355.

[25] Zhang X, Martina F, Ding J, Wang X, Williams SW. Fracture toughness and fatigue crack growth rate properties in wire + arc additive manufactured Ti-6Al-4V. Fatigue Fract Eng Mater Struct 2017;40:790–803. https://doi.org/10.1111/ffe.12547.

[26] Mu S, Li Y, Song D, Xu B, Chen X. Low cycle fatigue behavior and failure mechanism of wire arc additive manufacturing 16MND5 bainitic steel. J Mater Eng Perform 2021;30:4911–24. https://doi.org/10.1007/s11665-021-05554-1.

[27] Wächter M, Leicher M, Hupka M, Leistner C, Masendorf L, Treutler K, et al. Monotonic and fatigue properties of steel material manufactured by wire arc additive manufacturing. Appl Sci (Switzerland) 2020;10:5238. https://doi.org/10.3390/APP10155238.

[28] Rodideal N, Machado CM, Infante V, Braga DFO, Santos TG, Vidal C. Mechanical characterization and fatigue assessment of wire and arc additively manufactured HSLA steel parts. Int J Fatigue 2022;164:107146. https://doi.org/10.1016/j.ijfatigue.2022.107146.

[29] AWS A5 Committee on Filler Metals and Allied Materials. AWS A5.18/A5.18M: 2005 Specification for carbon steel electrodes and rods for gas shielded arc welding 2005.

[30] International Organization for Standardization. ISO 14341:2020 Welding consumables — Wire electrodes and weld deposits for gas shielded metal arc welding of non alloy and fine grain steels — Classification 2020.

[31] Bartsch H, Kühne R, Citarelli S, Schaffrath S, Feldmann M. Fatigue analysis of wire arc additive manufactured (3D printed) components with unmilled surface. Structures 2021;31:576–89. https://doi.org/10.1016/j.istruc.2021.01.068.

[32] Huang C, Li L, Pichler N, Ghafoori E, Susmel L, Gardner L. Fatigue testing and analysis of steel plates manufactured by wire-arc directed energy deposition. Addit Manuf 2023;73:103696. https://doi.org/10.1016/j.addma.2023.103696.

[33] Ermakova A, Razavi J, Berto F, Mehmanparast A. Uniaxial and multiaxial fatigue behaviour of wire arc additively manufactured ER70S-6 low carbon steel components. Int J Fatigue 2023;166:107283. https://doi.org/10.1016/j.ijfatigue.2022.107283.

[34] Zong L, Fang W, Huang C, Wang Z, Gardner L. Low cycle fatigue behaviour of wire arc additively manufactured ER70S-6 steel. Int J Fatigue 2023;176:107910. https://doi.org/10.1016/j.ijfatigue.2023.107910.

[35] Wang Z, Hou Y, Xu F. Experimental investigation on cyclic behaviour of wire arc additively manufactured carbon steel. Ce/Papers 2023;6:714–9. https://doi.org/10.1002/cepa.2507.

[36] Wang Z, Hou Y, Huang C, Han Q, Zong L, Chen M-T, et al. Experimental study and constitutive modelling of wire arc additively manufactured steel under cyclic loading. J Constr Steel Res 2024;213:108420. https://doi.org/10.1016/j.jcsr.2023.108420.

[37] Electro-Portugal. EUROTROD Welding Consumables 2015. http://www.electroportugal.com/downloads/file70_pt.pdf.

[38] Zhang T, Li H, Gong H, Wu Y, Chen X, Zhang X. Study on location-related thermal cycles and microstructure variation of additively manufactured inconel 718. J Mater Res Technol 2022;18:3056–72. https://doi.org/10.1016/j.jmrt.2022.03.178.

[39] Veiga F, Suárez A, Artaza T, Aldalur E. Effect of the heat input on wire-arc additive manufacturing of Invar 36 alloy: microstructure and mechanical properties. Weld World 2022;66:1081–91. https://doi.org/10.1007/s40194-022-01295-4.

[40] Rodrigues TA, Duarte V, Miranda RM, Santos TG, Oliveira JP. Current status and perspectives on wire and arc additive manufacturing (WAAM). Materials 2019;12: 1121. https://doi.org/10.3390/ma12071121.

[41] ASTM. ASTM E606/E606M-21 Standard test method for strain-controlled fatigue testing 2021.

[42] Branco R, Costa JD, Antunes FV. Low-cycle fatigue behaviour of 34CrNiMo6 high strength steel. Theor Appl Fract Mech 2012;58:28–34. https://doi.org/10.1016/j.tafmec.2012.02.004.

[43] Paul SK, Sivaprasad S, Dhar S, Tarafder S. Cyclic plastic deformation and cyclic hardening/softening behavior in 304LN stainless steel. Theor Appl Fract Mech 2010;54:63–70. https://doi.org/10.1016/j.tafmec.2010.06.016.

[44] Hirschberg MH, Manson SS, Smith RW. Fatigue behavior of materials under strain cycling in low and intermediate life range. 1963.

[45] Skelton RP, Maier HJ, Christ H-J. The Bauschinger effect, Masing model and the Ramberg-Osgood relation for cyclic deformation in metals. Mater Sci Eng A 1997; 238:377–90. https://doi.org/10.1016/S0921-5093(97)00465-6.

[46] Morrow J. Cyclic plastic strain energy and fatigue of metals. Internal Friction, Damping, and Cyclic Plasticity, ASTM. International 1965:45–87. https://doi.org/10.1520/STP43764S.

[47] Sivaprasad S, Paul SK, Das A, Narasaiah N, Tarafder S. Cyclic plastic behaviour of primary heat transport piping materials: Influence of loading schemes on hysteresis loop. Mater Sci Eng A 2010;527:6858–69. https://doi.org/10.1016/j.msea.2010.07.041.

[48] Masing G. Eigenspannungen und verfestigung beim messing. Zurich: Orell Fussliverlag; 1926. p. 332–5.

[49] Bai F-M, Zhou H-W, Liu X-H, Song M, Sun Y-X, Yi H-L, et al. Masing behavior and microstructural change of quenched and tempered high-strength steel under low cycle fatigue. Acta Metall Sin (Engl Lett) 2019;32:1346–54. https://doi.org/10.1007/s40195-019-00893-4.

[50] Plumtree A, Abdel-Raouf HA. Cyclic stress–strain response and substructure. Int J Fatigue 2001;23:799–805. https://doi.org/10.1016/S0142-1123(01)00037-8.

[51] Basquin OH. The exponential law of endurance tests. In: Proceeding Thirteen. Annu. Meet. II; 1910. p. 625–30.

[52] Coffin LFJr. A study of the effects of cyclic thermal stresses on a ductile metal. Trans. ASME 1954;76:931–50.

[53] Manson SS. Behavior of materials under conditions of thermal stress. National Advisory Committee for Aeronautics; 1954.

[54] Williams CR, Lee Y-L, Rilly JT. A practical method for statistical analysis of strain–life fatigue data. Int J Fatigue 2003;25:427–36. https://doi.org/10.1016/S0142-1123(02)00119-6.

[55] Smith KN, Watson P, Topper TH. A stress-strain function for the fatigue of metals. J Mater 1970;5:767–78.

[56] Łagoda T, Vantadori S, Głowacka K, Kurek M, Kluger K. Using the Smith-Watson-Topper parameter and its modifications to calculate the fatigue life of metals: the state-of-the-art. Materials 2022;15:3481. https://doi.org/10.3390/ma15103481.

[57] Lefebvre D, Ellyin F. Cyclic response and inelastic strain energy in low cycle fatigue. Int J Fatigue 1984;6:9–15. https://doi.org/10.1016/0142-1123(84)90003-3.

[58] Ellyin F, Kujawski D. An energy-based fatigue failure criterion. J Press Vessel Technol 1984;106:342–7. https://doi.org/10.1115/1.3264362.

[59] Liao D, Zhu S-P, Gao J-W, Correia J, Calçada R, Lesiuk G. Generalized strain energy density-based fatigue indicator parameter. Int J Mech Sci 2023;254:108427. https://doi.org/10.1016/j.ijmecsci.2023.108427.

[60] Jahed H, Varvani-Farahani A. Upper and lower fatigue life limits model using energy-based fatigue properties. Int J Fatigue 2006;28:467–73. https://doi.org/10.1016/j.ijfatigue.2005.07.039.

[61] de Jesus AMP, Matos R, Fontoura BFC, Rebelo C, Simões da Silva L, Veljkovic M. A comparison of the fatigue behavior between S355 and S690 steel grades. J Constr Steel Res 2012;79:140–50. https://doi.org/10.1016/j.jcsr.2012.07.021.

[62] Olmi G. Low cycle fatigue experiments on turbogenerator steels and a new method for defining confidence bands. J Test Eval 2012;40:539–52. https://doi.org/10.1520/JTE104548.

[63] Croccolo D, De Agostinis M, Fini S, Olmi G, Vranic A, Ciric-Kostic S. Influence of the build orientation on the fatigue strength of EOS maraging steel produced by additive metal machine. Fatigue Fract Eng Mater Struct 2016;39:637–47. https://doi.org/10.1111/ffe.12395.

[64] Ćirić-Kostić S, Croccolo D, De Agostinis M, Fini S, Olmi G, Paiardini L, et al. Fatigue response of additively manufactured Maraging Stainless Steel CX and effects of heat treatment and surface finishing. Fatigue Fract Eng Mater Struct 2022;45: 482–99. https://doi.org/10.1111/ffe.13611.

[65] Croccolo D, Bogojević N, De Agostinis M, Fini S, Olmi G, Robusto F, et al. Fatigue response of additively manufactured as-built 15–5 PH stainless steel and effects of machining and thermal and surface treatments. Fatigue Fract Eng Mater Struct 2023;46:433–51. https://doi.org/10.1111/ffe.13875.

[66] Croccolo D, De Agostinis M, Fini S, Olmi G, Bogojevic N, Ciric-Kostic S. Effects of build orientation and thickness of allowance on the fatigue behaviour of 15–5 PH stainless steel manufactured by DMLS. Fatigue Fract Eng Mater Struct 2018;41: 900–16. https://doi.org/10.1111/ffe.12737.

[67] Fisher RA. The design of experiments. London: Oliver & Boyd; 1935.

[68] Blanca MJ, Alarcón R, Arnau J. Non-normal data: Is ANOVA still a valid option? Psicothema 2017:552–7. https://doi.org/10.7334/psicothema2016.383.

[69] Hauser T, Reisch RT, Breese PP, Lutz BS, Pantano M, Nalam Y, et al. Porosity in wire arc additive manufacturing of aluminium alloys. Addit Manuf 2021;41: 101993. https://doi.org/10.1016/j.addma.2021.101993.

[70] Ayan Y, Kahraman N. Bending fatigue properties of structural steel fabricated through wire arc additive manufacturing (WAAM). Eng Sci Technol Internat J 2022;35:101247. https://doi.org/10.1016/j.jestch.2022.101247.